Motoaki Kimura
e-mail: kimura@mech.cst.nihon-u.ac.jp

Masahiro Takei

Department of Mechanical Engineering,
College of Science and Technology,
Nihon University,
8 Kanda Surugadai 1-Chome,
Chiyoda-ku
Tokyo 101-8308, Japan

Chih-Ming Ho
Mechanical and Aerospace Engineering
Department,
University of California,
Los Angeles, CA 90095

Yoshifuru Saito
Department of Electrical and Electronic
Engineering,
College of Technology,
Hosei University,
3-7-2 Kajino,
Koganei,
Tokyo 184-8584, Japan

Kiyoshi Horii
Shirayuri College,
1-25 Midorigaoka
Chiyoda-ku,
Tokyo 101-8308, Japan

Visualization of Shear Stress With Micro Imaging Chip and Discrete Wavelet Transform

The two-dimensional low-speed structure of a turbulent boundary layer has been clearly visualized by a combination of a shear stress sensor using micro electro mechanical systems and the discrete wavelet transform. The application of two-dimensional discrete wavelet transforms to the visualization of wall shear stress data obtained using the micro shear stress imaging chip is described. The experiment was carried out under various Reynolds number conditions. It is shown that it is possible to visualize the low-speed streak structure as contours of two-dimensional wavelet level corresponding to spanwise wave number as a function of Reynolds number. [DOI: 10.1115/1.1516599]

1 Introduction

The presence of near-wall shear stress streaks in turbulent boundary layers has been observed in flow visualization investigations, [1–5]. These streaks are typically very small at high Reynolds (Re) numbers and can not be properly resolved by traditional measurement techniques. Numerical simulations indicate that the streaks are associated with streamwise vortices in the viscous sublayer. The rotational motion of these vortices imposes high fluctuation surface shear stresses on the wall, [6]. Several techniques have been proposed for measuring shear stresses. The hot-film technique and its variants have been widely used in detailed investigations of fluctuating wall shear stress, [7,8]. The direction-sensitive laser Doppler anemometer is a technique that enables for the evaluation of both the magnitude and direction of the wall shear stress. The optical method proposed by Naquwi [9] is capable of measuring the wall shear stress at a high spatial resolution. However, an instrument with a fine spatial resolution, fast frequency response and high sensitivity for turbulent boundary layer research has not yet been developed.

The recent development of the micro electro mechanical systems (MEMS) manufacturing process has offered the possibility of sensing and controlling small near-wall streaks, [10]. A multidisciplinary research collaboration between UCLA and Caltech was initiated to design and fabricate a large-scale distributed control system with integrated micro-machined transducers and microelectronic circuits for surface shear stress control in turbulent boundary layers, [11,12].

However, the distribution of stripe structure with MEMS is an integral value composed of various frequency ingredients and can result in ambiguities in the stripe structure. Therefore, new techniques such as statistical and frequency analysis of the image data are necessary to perform detailed analysis. The stripe structure obtained with the micro-imaging chip is clearly visualized and analyzed using statistical methods, [13]. In terms of frequency analysis, the Fourier transform is a popular method but it removes the time-space information of the stripe structure.

Recent studies have investigated the use of the wavelet transform for time-space frequency analysis in mechanical engineering applications. The main advantage of wavelet analysis is its ability to analyze the frequency and not erase the time-space information. Wavelet transforms are classified as either continuous or discrete, [14]. Continuous wavelet transforms have been used for studies of time-frequency analysis in turbulent shear flow including self-similarity of a jet inner structure using one-dimensional continuous wavelets, [15], and scale transition in a mixing layer using two-dimensional continuous wavelets, [16]. In addition, most studies of time-frequency analysis use continuous wavelet transforms. Conversely, eddy motion in the atmospheric surface layer has been analyzed using the wavelet thresholding method, [17]. The analysis enables for an image to be decomposing and regenerated numerically according to the orthonormal transform. Saito [18] applied this principle to the analysis of electromagnetic waves.

The purpose of this paper is to describe the application of two-dimensional discrete wavelet transforms to the visualization of wall shear stress data obtained using a micro shear stress imaging chip. The stripe structure of shear stresses in a turbulent boundary layer is extracted for various frequency levels.

2 Experiments

2.1 Micro Shear Stress Imaging Chip. A micro shear stress imaging chip, which is composed of multiple thermal type sensors, [19], is shown in Fig. 1. The chip has three rows of micro sensors, each of which contain an array of 25 sensors. Figure 2 shows plan and cross-sectional views of the micro shear stress sensor. Each micro sensor consists of a $150 \times 3 \times 0.45$ μm polysilicon resistor, and a $200 \times 200 \times 1.2$ μm silicon nitride diaphragm that seals a 2 μm deep vacuum cavity. The purpose of the cavity is to reduce heat transfer from the resistor to the substrate and to increase the sensitivity of the sensor, [20]. The sensors are connected to external constant temperature mode circuits, which are used in the hot-wire anemometer, to drive at an overheat ratio of 1.1 through gold bonding wires. Output from the anemometer circuits is digitized by a 64-channel Keithly Metrabyte ADC board in a Pentium-based PC. The sensitivity of the shear stress sensor is approximately 1.0 V/Pa at a gain of 10.

2.2 Shear Stress Sensor Calibration and Temperature Compensation. The heating power of a shear stress sensor operating in steady state conditions can be correlated with wall shear stress τ as follows, [8]:

$$i^2 R^2 = (T_f - T)(A + B\tau^{1/3}) \tag{1}$$

where T_f and T are the temperature of the heated sensor and the measured fluid, respectively, R is the resistance of the sensor, i is the heating current passing through the sensor, and A and B are calibration constants. Two theoretical methods are used to correlate the output voltage with the wall shear stress τ. In the first method, τ in fully developed turbulent flow is related to the streamwise pressure gradient by

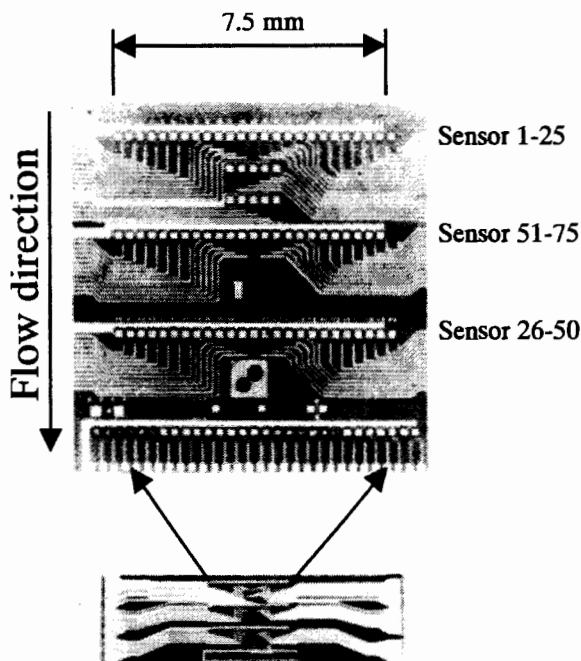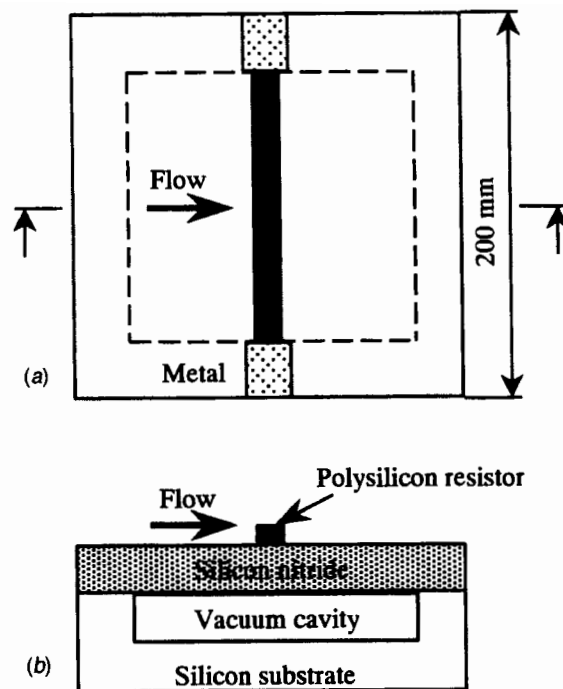$$dP_x/dx = -\tau/h \tag{2}$$

Fig. 1 Surface shear stress imaging chip

Fig. 2 Schematic plan (a) and cross-sectional (b) views of the micro shear stress sensor

where P_x is the local pressure, x is the streamwise coordinate, and h is the half-height of the wind channel. The pressure drop and output voltage of the sensor was measured at center velocities ranging from 8 to 20 m/s. If T is constant, the wall shear stress can be directly related to the output voltage E_o by a sixth-order polynomial as

$$\tau = a_0 + a_1 E_0 + \ldots + a_6 E_0^6 \tag{3}$$

where $a_0 a_1$, a_2, $\ldots a_6$ are calibration constants. These constants were calibrated in the channel flow in a downstream region in which turbulent flow was fully developed.

In the second method, an empirical relationship between Re and the wall shear stress in fully developed channel flow is obtained, [21], by using

$$u_\tau/u_\infty = 0.1079 \, \text{Re}^{-0.089} \tag{4}$$

and

$$\tau = u_\tau^2 \rho, \tag{5}$$

where u_τ is the friction velocity, u_∞ is the center velocity of the channel, Re ($= hu_\infty/\nu$, where h is the half-width of the channel and u_∞ is centerline velocity). The streamwise pressure gradient was measured and τ calculated using Eq. (2) and the second method given by Eqs. (4) and (5). Good agreement was observed between the two methods.

When T varies during the measurement process, a thermal correction should be applied. To determine the correction coefficient, previous micro shear stress sensor versus fine thermocouple simultaneous measurements have done in channel flow of 10 m/s at room temperatures ranging from 19.0 to 22.0°C. The slope of the sensor output/temperature curve was −310 mV/°C. Temperature compensation was achieved by collecting both ambient temperature and shear stress data and then performing an a posteriori correction using software.

2.3 Experimental Setup. This experiment was carried out in a turbulent channel flow facility. The channel, constructed of 13 mm Plexiglas, was 610 mm×25.4 mm in cross section and 4880 mm long. A DC axial blower was used to generate the airflow.

Previous hot-wire measurements suggested that a centerline channel flow of 10 m/s consists of laminar entrance flow and fully developed turbulent flow at the downstream half channel. The micro shear stress imaging chip was flush mounted on the channel wall 4267 mm from the inlet. One array consisting of 25 micro shear-stress sensors covering a distance of 7.5 mm was used to measure the instantaneous spanwise distribution of turbulent surface shear stress, Re ranged from 6960 to 17,400.

2.4 Shear-Stress Distribution. Statistical values, which are root mean square, skewness factor, and flatness factor of wall shear stress measured using the imaging chip, are confirmed, [22], to be similar to the data obtained in previous experiments, [7,23], and by numerical computation, [6]. Figure 3 shows the distribution of two-dimensional shear stresses. The horizontal axis spans 7.5 mm (data number 25), and the vertical axis spans 51.2 ms (data number 512) for three different values of Re. Each shear stress value was normalized by

$$\bar{\tau} = \frac{\tau - \tau_m}{\tau_{rms}} \tag{6}$$

using the mean shear stress. $_m$ root mean square shear stress. $_{rms}$ for each Re number as shown in Figs. 3(a), (b), and (c). The high shear stress regions are marked in red while blue represents shear stress with 11 contour colors. Figure 3(d) shows the original data
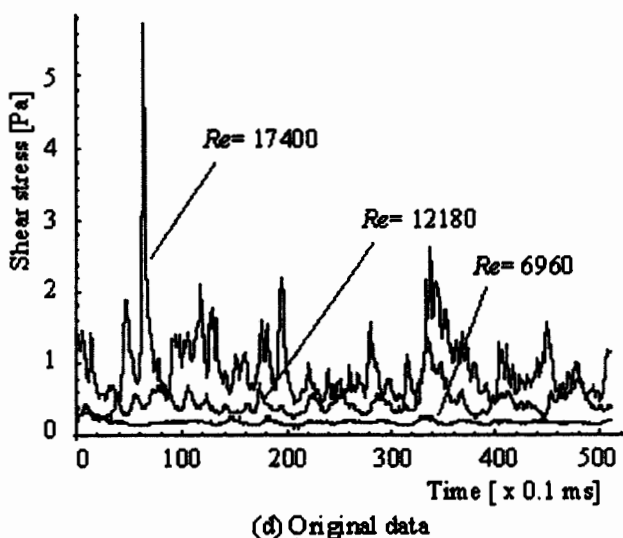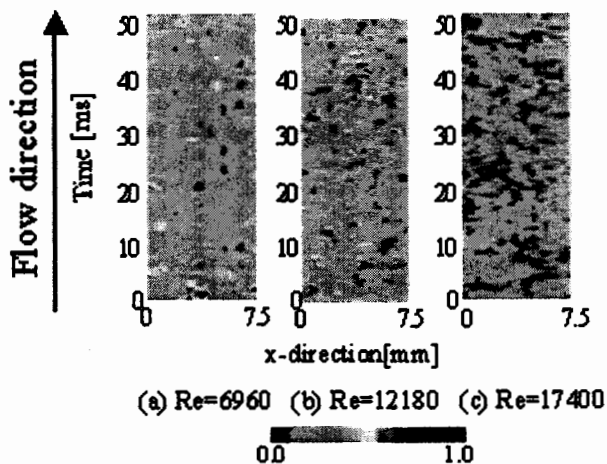
in the vertical direction at the point at which the maximum value was observed before normalization. The streaks were narrower, closer together, and appeared at shorter time intervals as Re increases. The shear stress fluctuation near to the wall increased rapidly, resulting in a significant peak in the turbulent boundary layer, because the velocity gradient increased rapidly due to the influence of eddies guided by bursting events. From Figs. 3(a) to (c), the red regions of Re=17,400 are insignificant and blue region is larger than those for lower Re number conditions.

3 Discussion

3.1 Spanwise Spacing of Low Speed Streaks. The characteristics of sublayer streaks are well documented. The streaks, which consist of low-speed fluid in the sublayer, appear randomly and are typically $1000\nu/u_\tau$ long in the streamwise direction, [24], with a mean spanwise spacing of $100\nu/u_\tau$, [5,25]. Here, ν and u_τ denote the kinematic viscosity and the wall shear velocity, respectively.

Next, the spanwise spacing of streaks was inspected by wave number spectrum with sensor data of 25 spanwise profiles as shown in Fig. 4. Low shear stress areas corresponding to low-speed streaks and high shear stress areas corresponding to kink parts of low-speed streaks were observed. Figure 5 shows an example of a spanwise wave number spectrum for the determination of the spanwise interval of streak structure. The figure shows the wave number spectrum for Re=6960. Local maxima at 200 and 300 [1/m] are not conspicuous peaks, but indicate a spanwise spacing interval of low speed streak. This result suggests that a spanwise spacing of low speed streaks is $99-150\nu/u_\tau$. Similar results were observed for a range of Re numbers. It is concluded that this value verifies the result of $100\nu/u_\tau$ obtained from visualization experiments.

3.2 Streamwise Wave Number Decomposition

3.2.1 Analysis Method and Results Using Two-Dimensional Discrete Wavelet Multiresolution Analysis. The original data was derived from 25 data points over 512 epochs. The 25 points were extrapolated to 32 points (4 on the right side and 3 on the left side) with Fourier series coefficients in order to afford the power of two for the discrete wavelet transform. The values of the original points, which are points 5 to 29 in the extrapolated coordinate system, were extracted after the calculation. The extrapolated length measured 9.6 mm (300 μm×32). In the case of the 16 input data and fourth-order Daubechies functions, multiresolution analysis outputs Level 0 to Level 3. The two-dimensional wavelet spectrum S was obtained from

$$S = W_n X W_m^T \tag{7}$$

(a) Re=6960 (b) Re=12180 (c) Re=17400

(d) Original data

Fig. 3 Shear stress measured with the imaging chip; (a) Re =6960, (b) Re=12,180, (c) Re=17,400, (d) original data

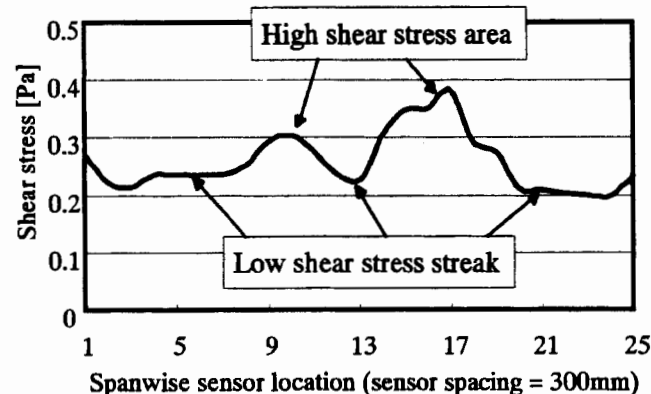Spanwise sensor location (sensor spacing = 300mm)

Fig. 4 Shear stress distribution in spanwise direction (Re =6960)
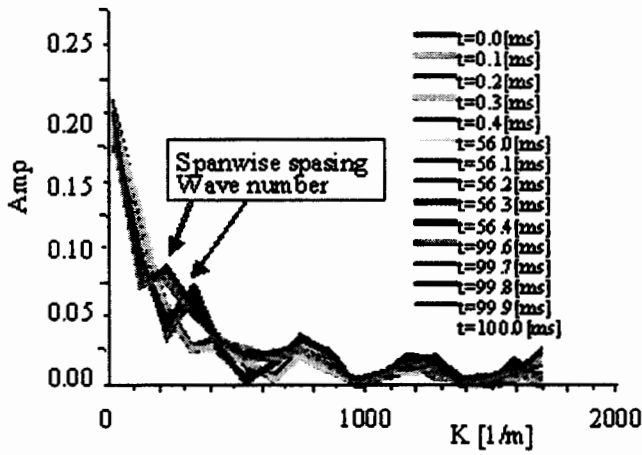
Fig. 5 Wave number spectrum of shear stress distribution in spanwise direction (Re=6960)

Fig. 7 Time frequency of 16th Daubechies

where W_m^T is a transpose of W_n. From Eq. (7), the discrete inverse wavelet transform is expressed by

$$X = W_n^T S W_m. \tag{8}$$

In this study, a 16th-order Daubechies function was used as the analyzing wavelet. A multiresolution analysis was performed using the inverse wavelet transform in Eq. (8), after the wavelet transform in Eq. (7) was operated to 25×512 shear stress distribution data in Fig. 3. In the case of the sixteenth-order Daubechies function and $512 \ (= 2^9)$ time data (total measurement time $= 51.2$ ms), the multiresolution analysis with respect to time classifies to seven levels as shown in

$$X = W_n^T S W_m = W_n^T S_0 W_m + W_n^T S_1 W_m + W_n^T S_2 W_m + W_n^T S_3 W_m$$
$$+ W_n^T S_4 W_m + W_n S_5 W_m + W_n^T S_6 W_m. \tag{9}$$

In Eq. (9), $W_n^T S_0 W_m$ is denoted Level 0, which indicates the lowest frequency, $W_n^T S_6 W_m$ is denoted Level 6, which indicates the highest frequency. In data point 32, the wavelet level of the multiresolution was decomposed from level 0 to level 3. The absolute values by Fourier transform and wavelets are shown in Fig. 6 and Fig. 7. Each level operates a form of band pass filter.

Figures 8, 9, and 10 show the multiresolution with nine contours for low Re number, middle Re number, and high Re number conditions, respectively. Low shear stresses are denoted blue and high shear stresses are denoted red. Minus values are produced because the values were normalized. Level 6 is not shown because noise was dominant. The patterns adding all levels from Level 0
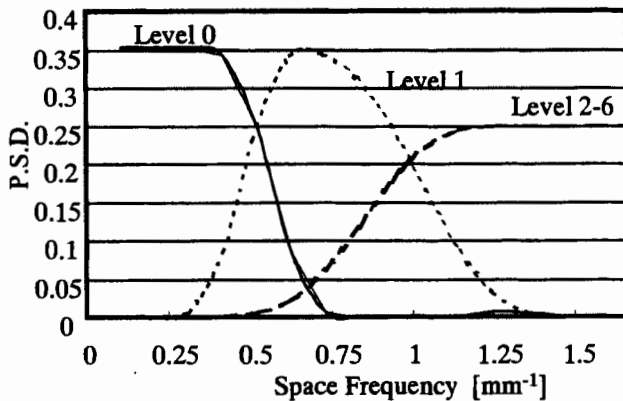

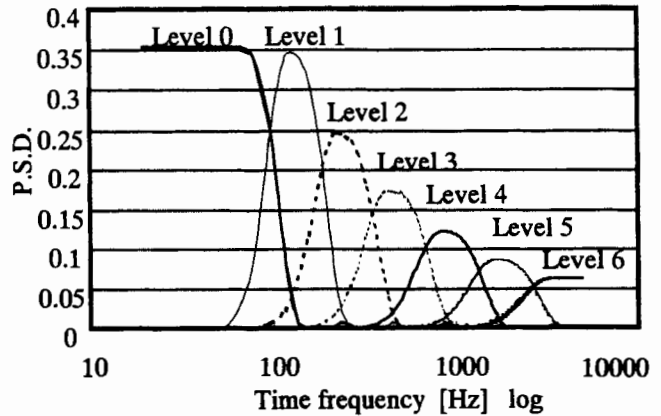Fig. 6 Space frequency of 16th Daubechies

to Level 6 enable the complete recovery of the original shear stress distributions in Fig. 3, because Daubechies analyzing wavelets are orthonormal functions. The relation between the representative frequency, which was calculated with the maximum P.S.D. in Figs. 6 and 7, and each wavelet level is shown in Table 1 and Fig. 11.

From these figures, the original input data were decomposed from the low-frequency component Level 0 to the high-frequency component Level 5. I have done the above section of spanwise spacing of low-speed streaks, if spanwise spacing is around 100 times of the wall unit, the spanwise wave number corresponding to Re=6960 and 17,400 becomes 0.24 mm^{-1} and 0.61 mm^{-1}, respectively. Level 0 shows a low-speed domain in Re=6960 and level 1 corresponds to Re=17,400. The stripe structures due to a series of bursting events in the low-speed shear stress area are visualized clearly for each frequency level without erasing the time and space information. In particular, red and green regions appear more clearly on Levels 0 and 1 for low Re numbers. The shear stress distribution appears until Level 3 and wave patterns are observed on Levels 4 and 5.

3.2.2 Discussion According to the Kolmogorov Turbulence Theory. The relation between wavelet level and wave number is discussed by application of the Kolmogorov turbulence theory to

Table 1 Relation between wavelets level and representative frequency

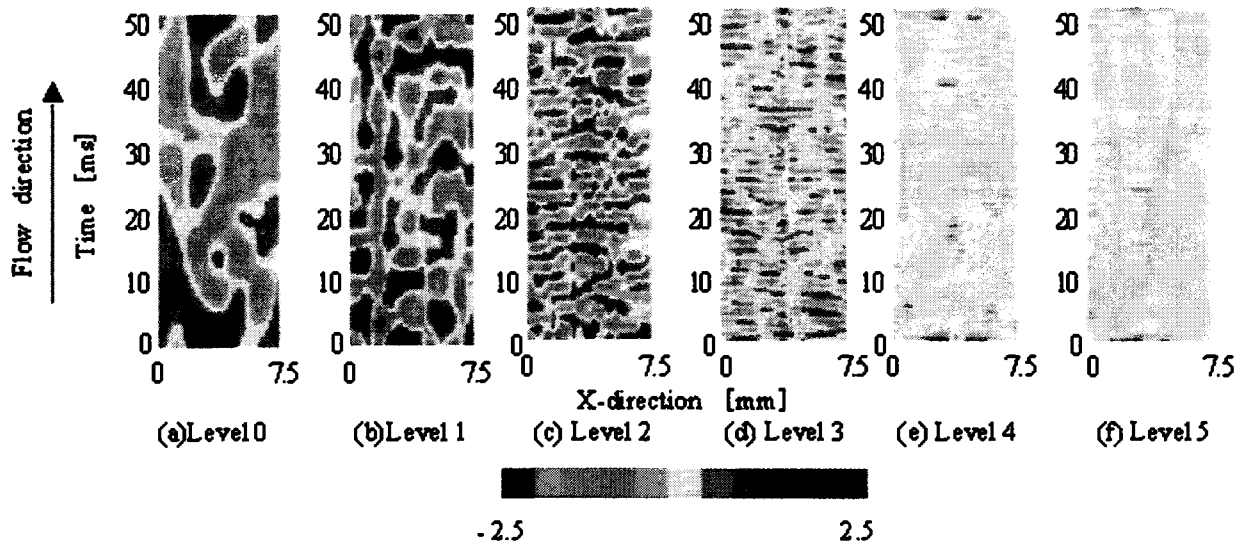|	Time frequency	Space frequency
Representative frequency on Level 0	2.0×10^1 [Hz]	1.04×10^{-1} [mm^{-1}]
Representative frequency on Level 1	1.4×10^2 [Hz]	7.00×10^{-1} [mm^{-1}]
Representative frequency on Level 2	2.3×10^2 [Hz]	
Representative frequency on Level 3	4.5×10^2 [Hz]	
Representative frequency on Level 4	8.8×10^2 [Hz]	1.2×10^0 [mm^{-1}]
Representative frequency on Level 5	1.7×10^3 [Hz]	
Representative frequency on Level 6	4.7×10^3 [Hz]	
Maximum frequency on Level 6 f_{max}	4.7×10^3 [Hz]	1.6×10^0 [mm^{-1}]

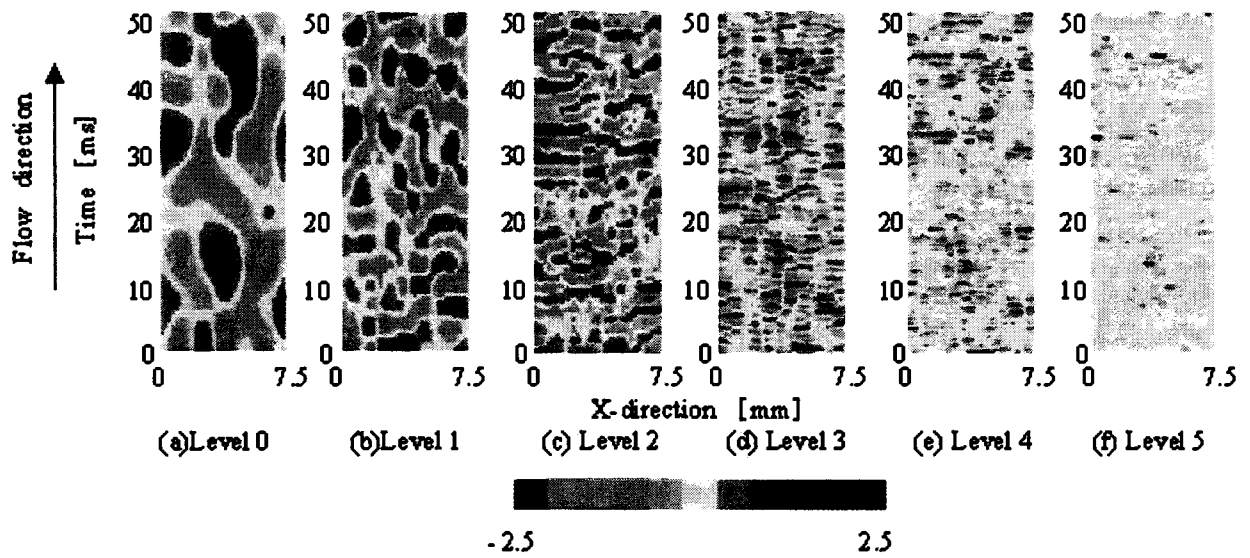**Fig. 8 Wavelets multiresolution in Re=6960**

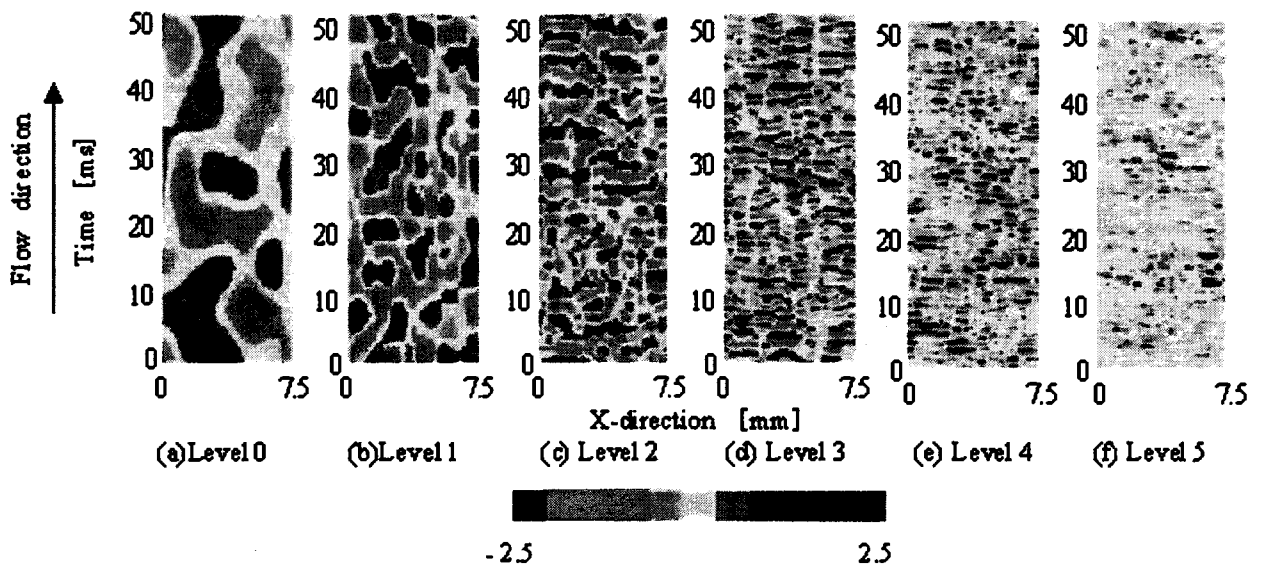**Fig. 9 Wavelets multiresolution in Re=12,180**

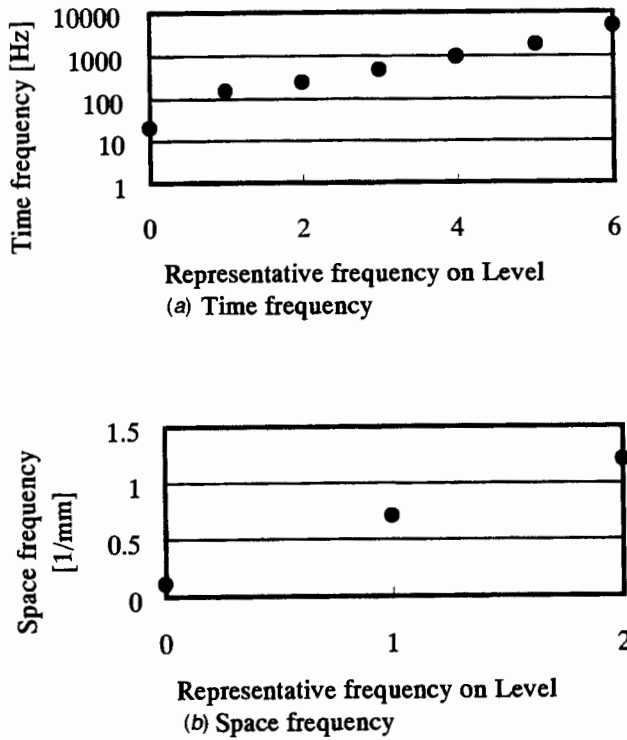**Fig. 10 Wavelets multiresolution in Re=17,400**

Fig. 11 Relation between wavelets level and representative frequency

the time axis of discrete wavelet multiresolved resolution. The Kolmogorov wave number k_k that indicates the highest viscous dispersion rate is expressed by

$$k_k = \left(\frac{\varepsilon}{\nu^3} \right)^{1/4} \quad (10)$$

where ν is the kinematic viscosity, ε is the energy transportation rate, that is

$$\varepsilon = A \frac{\nu_0^3}{l_0}$$

$$\nu_0 = 0.2\bar{\nu} \quad (11)$$

Table 2 Relation between wavelet level and representative wave number

|	$v=8m/s$ $Re=6960$	$v=14m/s$ $Re=12180$	$v=20m/s$ $Re=17400$
Representative wavenumber on Level 0	7.7 ×10⁻¹[cm⁻¹]	4.4 ×10⁻¹[cm⁻¹]	3.1 ×10⁻¹[cm⁻¹]
Wavenumber in energy contain region k_0	8.0 ×10⁻¹[cm⁻¹]	8.0 ×10⁻¹[cm⁻¹]	8.0 ×10⁻¹[cm⁻¹]
Representative wavenumber on Level 1	5.4 ×10⁰[cm⁻¹]	3.1 ×10⁰[cm⁻¹]	2.1 ×10⁰[cm⁻¹]
Representative wavenumber on Level 2	9.2 ×10⁰[cm⁻¹]	5.3 ×10⁰[cm⁻¹]	3.7 ×10⁰[cm⁻¹]
Representative wavenumber on Level 3	1.8 ×10¹[cm⁻¹]	1.0 ×10¹[cm⁻¹]	7.1 ×10¹[cm⁻¹]
Representative wavenumber on Level 4	3.4 ×10¹[cm⁻¹]	2.0 ×10¹[cm⁻¹]	1.4 ×10¹[cm⁻¹]
Representative wavenumber on Level 5	6.7 ×10¹[cm⁻¹]	3.9 ×10¹[cm⁻¹]	2.7 ×10¹[cm⁻¹]
Representative wavenumber on Level 6	1.9 ×10²[cm⁻¹]	1.0 ×10²[cm⁻¹]	0.7 ×10²[cm⁻¹]
Maximum wavenumber on Level 6 k_{max}	1.96 ×10²[cm⁻¹]	1.12 ×10²[cm⁻¹]	0.79 ×10²[cm⁻¹]
Kolmogorov wavenumber k_k	3.49 ×10²[cm⁻¹]	2.67 ×10²[cm⁻¹]	1.76 ×10²[cm⁻¹]
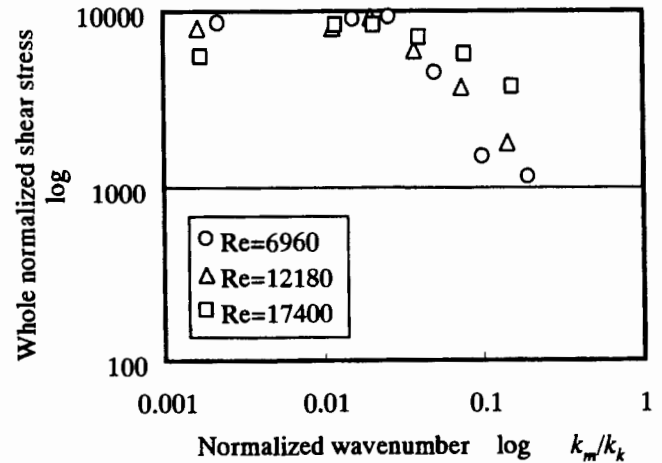
Fig. 12 Relation between whole normalized shear stress and wavenumber on the time space

where ν_0 is a representative velocity fluctuation that is assumed to be 0.2 times the mean velocity $\bar{\nu}$, and l_0 is a length scale in the energy contain region that is assumed to be the radius of the pipeline. In this study, the constant A is assumed to be 1.0. The representative wave number on wavelet level m is obtained by

$$k_m = \frac{2\pi f_R}{\nu_0} \quad (12)$$

where f_R is a representative frequency, which is the maximum power spectrum density in Fig. 7. The relation between the wavelet level and the representative wave number is shown in Table 2. From this table, Level 0 indicates a wave number under the energy contain region, and Level 6 indicates the vicinity of k_k. The wavelet level covers from the energy contain region to the viscous dispersion region.

In the following section, all shear stresses on each wavelet level are defined by

$$\overline{\tau_{all}} = \sum_{j=1}^{512} \sum_{i=1}^{25} \sqrt{(\overline{\tau_{ij}})^2} \quad (13)$$

to consider the relation between the stress and Re. i is a position on the time axis, j is a position on the space axis. The results are shown in Fig. 12. The horizontal axis is the representative wavenumber in Table 1 normalized using k_k.

In this figure, the shear stress maintains an approximately constant value until wave number 0.02, which is equivalent to Level 2 irrespective of Re. This is because the wave number is near to the energy contain region from Table 2. However, at wave numbers greater than 0.02, the total shear stress decreases as the wave number increases. Moreover, the shear stress dramatically decreases for low values of Re. This is because the eddy dispersion is significantly influenced by the viscosity in low Re regions. The proposed visualization technique is therefore verified.

4 Conclusions

A micro shear-stress imaging chip was used to measure the instantaneous shear-stress distribution in a turbulent wall boundary layer in flow with Reynolds number ranging from 6960 to 17,400. The two-dimensional shear stress distributions were visualized with a two-dimensional discrete wavelet transform. The following conclusions are proposed:

1. The two-dimensional structure of wall shear stress can be decomposed and clearly visualized on each frequency level without erasing time-space information using two-dimensional wavelet multiresolution analysis.

2. It is possible to visualize the low speed streak structure on the wall as contours of two-dimensional wavelet level corresponding to spanwise wave number as a function of Re number.

3. The total shear stresses under Level 2 relevant to near energy contain region maintains the same value irrespective of Re number. However, the total shear stress over Level 3 in near viscous dispersion regions under low Re number conditions is lower than that under high Re number conditions. This is a reasonable observation because the structure is significantly influenced by viscosity under low Re number conditions.

Acknowledgments

References

[1] Kim, H. T., Kline, S. J., and Reynolds, W. C., 1971, "The Production of Turbulence Near a Smooth Wall in a Turbulent Boundary Layer," J. Fluid Mech., **50**, Part 1, pp. 133–160.

[2] Falco, R., 1980, "The Production of Turbulence Near a Wall," AIAA Paper No. 80-1356.

[3] Cantwell, B. J., 1981, "Organized Motion in Turbulent Flow," Annu. Rev. Fluid Mech., **13**, pp. 457–515.

[4] Head, M. R., and Bandyopadhyay, P., 1981, "New Aspects of Turbulent Boundary-Layer Structure," J. Fluid Mech., **107**, pp. 297–338.

[5] Smith, C. R., and Metzler, S. P., 1983, "The Characteristics of Low-Speed Streaks in the Near-Wall Region of a Turbulent Boundary Layer," J. Fluid Mech., **129**, pp. 27–54.

[6] Kim, J., Moin, P., and Moser, R., 1987, "Turbulent Statistics in Fully Developed Channel Flow at Low Reynolds Number," J. Fluid Mech., **177**, pp. 133–166.

[7] Alfredsson, P. H., Johansson, A. V., Haritonidis, J. H., and Eckelmann, H., 1988, "The Fluctuating Wall-Shear Stress and the Velocity Field in the Viscous Sublayer," Phys. Fluids, **31**, pp. 1026–1033.

[8] Bruun, H. H., 1995, "Hot-Wire Anemometry," Oxford University Press, Oxford, UK, pp. 272–286.

[9] Naqwi, A. A., and Reynolds, W. C., 1991, "Measurement of Turbulent Wall Velocity Gradients Using Cylindrical Waves of Laser Light," Exp. Fluids, **10**, pp. 257–266.

[10] Ho, C. M., Tung, S., and Tai, Y. C., 1996, "Interactive Control of Wall Structures by MEMS-Based Transducers," Advances in Turbulence, Proceedings of the Sixth European Turbulence Conference, Lausanne, Switzerland, July, p. 413.

[11] Tung, S., Hong, H., Huang, J. B., Ho, C. M., Liu, C., and Tai, Y. C., 1995, "Control of a Streamwise Vortex by a Mechanical Actuator," Proceedings of 10th Symposium on Turbulent Shear Flows, **1**, Pennsylvania, Aug., pp. 1–19.

[12] Ho, C. M., Tung, S., Lee, G. B., Tai, Y. C., Jiang, F., and Tsao, T., 1997, "MEMS-A Technology for Advancements in Aerospace Engineering," AIAA Paper No. 97-0545.

[13] Kimura, M., Tung, S., Ho, C. M., Jiang, F., and Tai, Y. C., 1997, "MEMS for Aerodynamic Control," 28th AIAA Fluid Dynamics Conference, AIAA Paper No. 97-2118.

[14] Morlet, F., 1982, "Wavelets Propagation and Sampling Theory," Geophysics, **47**, pp. 203–236.

[15] Everson, R., and Sirovich, L., 1990, "Wavelets Analysis to the Turbulence Jet," Phys. Lett., **145**, pp. 314–322.

[16] Dallard, T., and Spedding, G. R., 1993, "2-D Wavelet Transforms: Generalisation of the Hardy Space and Application to Experimental Studies," Eur. J. Mech. B/Fluids, **12**, pp. 107–134.

[17] Katul, G., and Vidakovic, B., 1998, "Identification of Low-Dimensional Energy-Containing/Flux Transporting Eddy Motion in the Atmospheric Surface Layer Using Wavelet Thresholding Methods," J. Atmos. Sci., **55**, pp. 377–389.

[18] Saito, Y., 1996, "Wavelets Analysis for Computational Electromagnetics, (in Japanese)," Trans. Inst. Electr. Eng. Jpn., Part A, **116A**, pp. 833–839.

[19] Jiang, F., Tai, Y. C., Gupta, B., Goodman, R., Tung, S., Huang, J. B., and Ho, C. M., 1996, "A Surface-Micromachined Shear Stress Imager," Proceedings of the 9th International IEEE Workshop on MEMS, San Diego, CA, p. 110.

[20] Huang, J. B., Tung, S., Ho, C. H., Liu, C., and Tai, Y. C., 1996, "Improved Micro Thermal Shear-Stress Sensor," IEEE Trans. Instrum. Meas., **45**, pp. 570.

[21] Hussain, A. K. M. F., and Reynolds, W. C., 1970, "The Mechanics of a Perturbation Wave in Turbulent Shear Flow," Air Force Office of Scientific Report, 70-1655TR, pp. 29–33.

[22] Kimura, M., Tung, S., Lew, J., Ho, C. M., Jiang, F., and Tai, Y. C., 1999, "Measurements of Wall Shear Stress of a Turbulent Boundary Layer using a Micro-Shear-Stress Imaging Chip," Fluid Dyn. Res., **24**, pp. 329–342.

[23] Obi, S., Inoue, K., Furukawa, T., and Masuda, S., 1995, "Experimental Study on the Statistics of Wall Shear Stress in Turbulent Channel Flows," Proceedings of 10th Symposium on Turbulent Shear Flows, **1**, pp. 5-19–5-24.

[24] Moin, P., and Kim, J., 1982, "Numerical Investigation of Turbulent Channel Flow," J. Fluid Mech., **118**, pp. 341–377.

[25] Kline, S. J., Reynolds, W. C., Schraub, F. A., and Runstadler, P. W., 1967, "The Structure of Turbulent Boundary Layers," J. Fluid Mech., **30**, pp. 741–773.